Supplement of Atmos. Chem. Phys., 22, 6365–6391, 2022
https://doi.org/10.5194/acp-22-6365-2022-supplement

Supplement of

An evaluation of new particle formation events in Helsinki during a Baltic Sea cyanobacterial summer bloom

Roseline C. Thakur et al.

Correspondence to: Roseline C. Thakur (roseline.thakur@helsinki.fi)

Back trajectory calculations

Back trajectories of the different NPF event days were calculated using the data from the Global data Assimilation System (GDAS) as input into the NOAA Hybrid Single-Particle Lagrangian Integrated Trajectory (HYSPLIT) model (http://www.arl.noaa.gov/ready/, Rolph et al., 2017; Stein et al., 2015). We used the isentropic trajectories as they incorporate vertical transport components. The 24 h back trajectories were calculated at an arrival height of 100 m a.g.l. The new trajectory starts every 6 hours. The frequency (%) of trajectory was calculated with the following equation (Eq. (1)).

$$\text{Traj. Freq.} = \frac{100 \times number\ of\ trajectories\ passing\ through\ each\ grid\ square}{number\ of\ trajectories} \quad (1)$$

The trajectory analysis was also performed using the Lagrangian particle dispersion model Flexpart v10.4 (Pisso et al., 2019; Stohl et al., 2005) mainly to assess the residence times of the air masses. Flexpart is a stochastic model used to compute trajectories of hypothetical particles, based on mean as well as turbulent and diffusive flow (Pisso et al., 2019). We have used Flexpart along with ECMWF ERA-Interim wind-fields which has a spatial resolution of 1°×1° at three hour temporal resolution (Pisso et al., 2019). Flexpart was used to simulate 3-days backward trajectories starting from the particle release point located at SMEAR III (24.5° E, 60.1° N) for the event days. The residence times were normalized for clarity in all the figures and is shown on a scale of 0 to 1.

Meteorological and other supporting data

The meteorological data such as wind speed, wind direction, temperature, pressure, relative humidity and other supporting datasets e.g chlorophyll (Chl-*a*), SO_2, O_3 concentration and sea level information was additionally used to interpret the NPF events and support the observations of this work (See table S1 for details). All the meteorological parameters are measured by sensors installed on the roof of the physicum building (where CI-APiTOF was housed). Thus we can say that the precursor vapor concentrations measured by the CI-APiTOF was not influenced by any vertical mixing of air masses since the sensors for meterological parameters (installed on the roof of 5th floor, physicum building and CI-APiTOF (installed on the 4th floor, physicum building) was almost at the same height. However, the measurements for particle size distributions was carried out at SMEAR III, which is 25 m a.m.sl and the wind vane at the physicum building was situated roughly at 50 m a.m.s.l. ,we state that the particle size distribution data might not be completely free from downward vertical mixing of air mass and should be treated with certain uncertainty. However, near the SMEAR III station, the mixing usually affected the larger particles, decreasing their number concentration (Järvi et al., 2009). So we can assume that the uncertainties in the number concentration of nucleation and Aitken mode particles would be negligible in this study.

The Chl*a* satellite images were mapped through the GlobColour level-3. The GlobColour level-3 mapped products present merged data from SeaWIFS, MERIS, MODIS AQUA, VIIRS (O'Reily et al., 2000) sensors to provide robust and high coverage data for Chl-*a* measurements. The merging processes are described in Mangin and d'Andon, 2017. In this study, weighted average method (AVW) for retrieving daily Chl*a* concentration (mg m^{-3}) for latitude: 45 °N to 80 °N and longitude: 20 °W to 60 °E was used. The GlobColour level-3 binned products have a resolution of 1/24° at the equator (i.e. around 4.63 km) for global products (Mangin and d'Andon, 2017). However this resolution is not high enough to demarcate the contribution of Chl*a* from cyanobacteria and macroalgae in the marine region. Nonetheless, the contribution of macrolagae to Chl*a* still holds a significant place since the Baltic Sea and other regions of Gulf of Finland that are abundant in microalgae.

Table S1 Details of Instruments and other supporting data

Parameter measured	**Technique**	**Instrument**	**Resolution and detection limits**	**Site of Measurement**
SO_2	UV-fluorescence technique	Horiba APSA 360	60 s detection limit: 0.2 ppb	a
NO_x	Chemiluminescence technique + thermal (molybdenum) converter	TEI42S	60 s detection limit: 0.2 ppb	a
O_3	IR-absorption photometer	TEI 49	60 s detection limit: 0.5 ppb	a
Air Temperature	Platinum resistance thermometer	Pt-100	60 s	b
Wind direction	2-D ultrasonic anemometer	Thies Clima ver. 2.1x	10 s	b
Wind Speed	Platinum resistance thermometer + thin film polymer sensor	Vaisala DPA500	4 min	b
Relative humidity	Platinum resistance thermometer + thin film polymer sensor	Vaisala DPA500	4 min	b
Global Radiation	Net radiometer	Kipp & Zonen CNR1	60s	b
Tidal Height	wave buoys		c	Helsinki Suomenlina, Gulf of Bothnia, Northern Baltic Sea

[a] SMEAR III station

[b]roof of university of Helsinki (UHEL) Building (kumpula campus)

[c]Wave height is the vertical difference between the wave through and the wave crest. The significant wave height is calculated as the average of one third of the highest waves from the energy spectrum.

Formation and growth rate calculations

The growth rates (GRs) were calculated based on the 50% appearance time method using the NAIS ion data from both polarities, depending on the better quality polarity (Dada et al., 2020; Dal Maso et al., 2016; Lehtipalo et al., 2014). This method uses particle number concentration at different size bins (D*p*), which are recorded as a function of time. The "appearance time" of particles of size D*p* is the time when their number concentration reaches 50% of its maximum value during the NPF event. To estimate the maximum GR (kinetic) that can be explained by the condensation of certain vapors, two parametrization methods were used, first by Nieminen et al., 2010 for IA and MSA and the second by Stolzenburg et al., 2020 for SA. The growth estimation from SA condensation recently provided by Stolzenburg et al., 2020 also takes into account the hydration of SA particles and dipole-dipole enhancement which is responsible for increasing the collision rate between neutral molecules and neutral particles. As these parameters were not known for IA and MSA, we used the method by Nieminen et al. (2010) for them. The growth due to MSA could be slightly overestimated by this method (Beck et al., 2021) since the parameterization is based on the assumption of irreversible condensation, but MSA rapidly partitions between gas and particle phases if suitable meteorological conditions prevail. The calculated kinetic GR was compared with the total measured particle GR to determine the contribution of each vapor to the growth process (discussed in further sections).

The formation rate of the total particles of mobility diameter 1.5 nm is calculated using the time derivative of the particle number concentration measured using the PSM in the size range 1.5– 3 nm. The formation rate was corrected for the coagulation losses and growth out of the bin following the method explained by Kulmala et al. 2012. The formation rate of the charged particles was calculated from the time derivative of ions measured using the NAIS in ion mode in size range 1.5–3 nm from both polarities. The formation rate of ions was corrected for coagulation sink, growth outside of the bin, ion-ion recombination and ion-neutral attachment as previously discussed in Kulmala et al. 2012.

The cloudiness parameter

It is defined as the ratio of measured global radiation (R_d) divided by the theoretical global irradiance (R_g):

$$P = \frac{R_d}{R_g}$$

The theoretical maximum of global radiation (R_g) is calculated by taking into consideration the latitude of the measurement station and the seasonal solar cycle. $P < 0.3$ defines a complete cloud coverage and $P > 0.7$ defines clear-sky conditions. This classification is followed by many previous studies (Perez et al., 1990; Sogacheva et al., 2008; Sánchez et al., 2012).

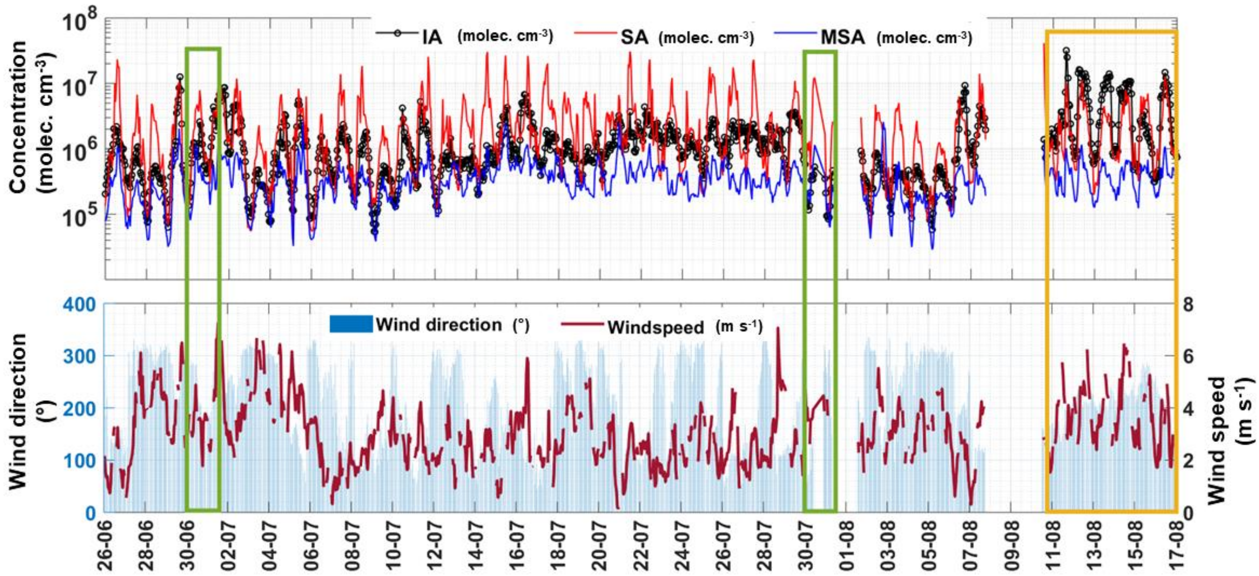

Figure S1: Time series concentration of SA, MSA and IA (60min averaged data) and their variability with changing wind speed and wind direction (30min averaged data). The green boxes denote the local events and yellow box is covers the time period when the burst/spike events were observed during the study.

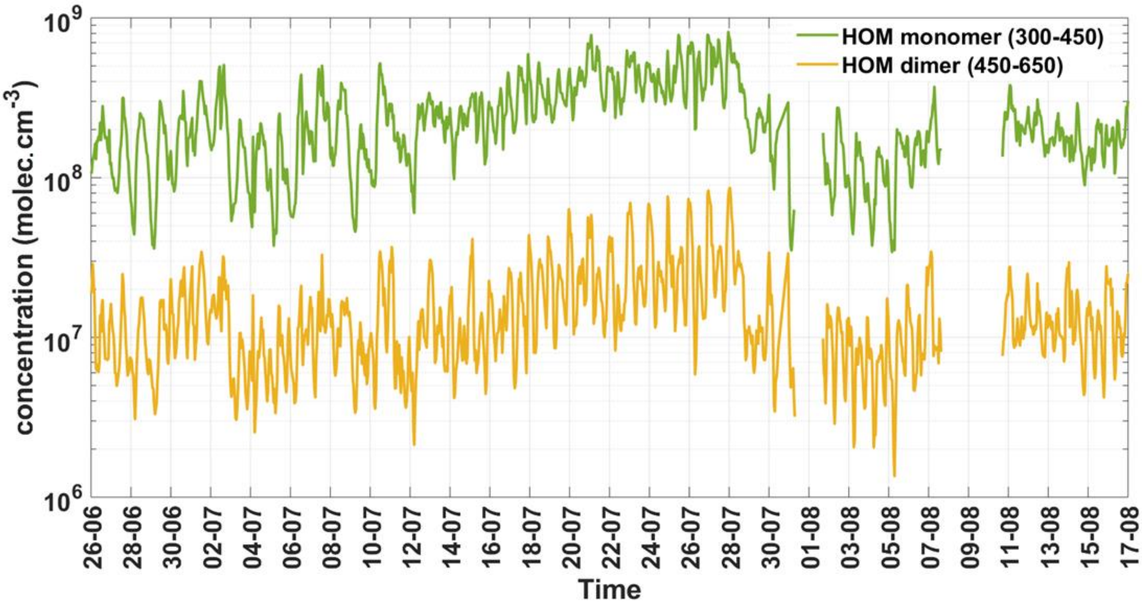

Figure S2: Time series variability in HOM monomer (sum of mass range 300–450 m/z) and dimer (sum of mass range 450-650 m/z) concentration during the study period (60min averaged data from CI-ApiToF)**.** Note the concentrations are plotted using the unit mass resolution data.

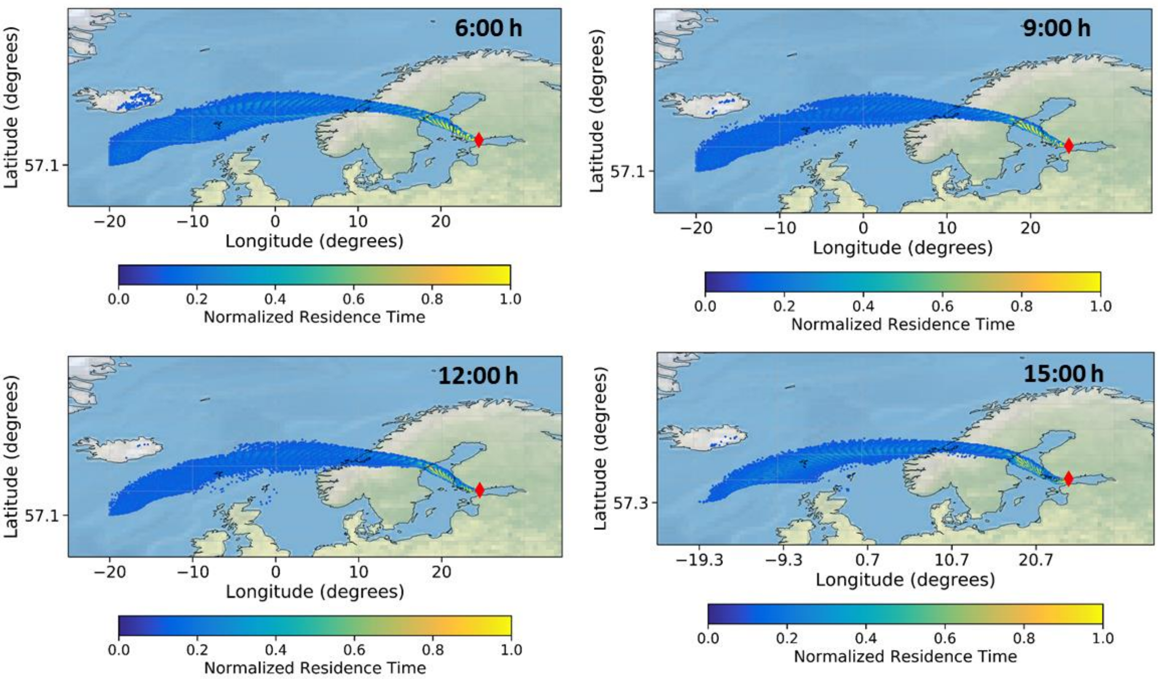

Figure S3: Normalized residence times of air masses (3-day backwards) arriving at the experimental site on 30 June 2019. The color bar indicates the normalized residence times for each subplot. The residence time of particles originating 3 days before reaching SMEAR III is shown for 6:00 h, 9:00

h, 12:00 h and 15:00 h. The red shaded areas indicate the latitude/longitude pairs having the maximum residence time.

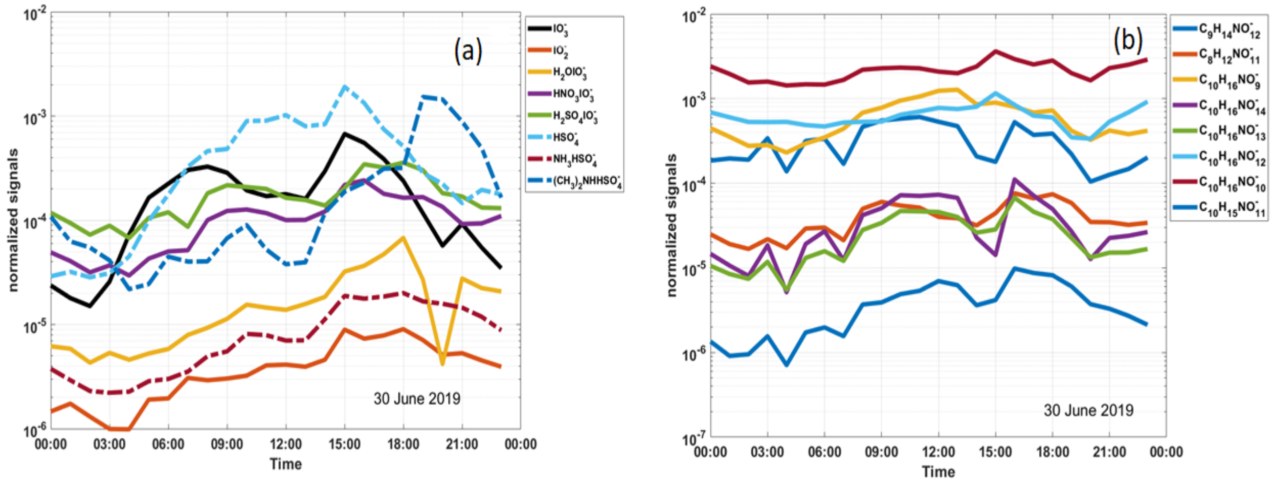

Figure S4: Diurnal variation of the inorganic clusters (a) and organic clusters (b) observed during the NPF event on 30 June 2019 as seen from the spectrum of CI-ApiToF.

Local/regional event 30 July 2019

Another local/regional event was observed on 30 July 2019 (Fig. S5a), forming particles, which grew to almost CCN relevant sizes. The growth of ions and particles occurred from 07:45 h-11:15 h (Fig. S5a and S5b). By this time, the particles had reached around 50 nm in size (lower limit of CCN). The highest $J_{1.5}$ (3.7 cm^{-3} s^{-1}) was observed at 09:00 h, significantly higher than J (ions), indicative of a neutral nucleation event (Fig. S5c). After 11:30 h, we observe a group of fragmented burst or spike events without clear growth pattern. No significant variation in formation rates was observed in the positive and the negative modes (Fig. S5b). A clear increase in sub-3 nm (1.25–3.1 nm) particle concentration (from 10^2 to $>10^3$) is seen during this event and formation rate ($J_{1.5}$) of the smallest particles increases from 0.9 cm^{-3} s^{-1} to 3.8 cm^{-3} s^{-1} between 06:00 -09:00 h indicating cluster formation (neutral nucleation) (Fig. S5c). A 10 times increase in sub 3nm particles is observed once the cluster formation initiated (07:45 h, local time UTC+2 h) when the concentration of SA increases from 8.2×10^6 to 1.2×10^7molec. cm^{-3} and the nucleation mode particles shows a significant increase from ~2000 cm^{-3} to ~10 000 cm^{-3} during the event, however we do not see any significant increase in aitken and accumulation mode particles (Fig. S5e). The aitken mode particle concentration starts to increase after a time lag of 40 min. Unfortunately, in this case we cannot discuss on the SA concentration after 12:00 h as data recording was disrupted between 12:30-20:30 h. The highest SA concentration during this event was 1×10^7 molec cm^{-3} as compared to IA and MSA which were one order of magnitude lower than SA (1×10^6 and 5×10^6 molec. cm^{-3}, respectively) (Fig. S5d). The particles reached the size of 40 nm at around 11:30 h after which the event ceases. The accumulation mode particles remain more or less constantly low, yet we observe a disruption in the event. A change in wind direction from 120° to 200° was observed between 11:30–12:30 h, which lead to the observation that we do not see regional NPF (growing particles) in the changed air mass. The cynobacteria bloom on 30 July 2019 was not much spread in the sea areas (Fig. S5f).

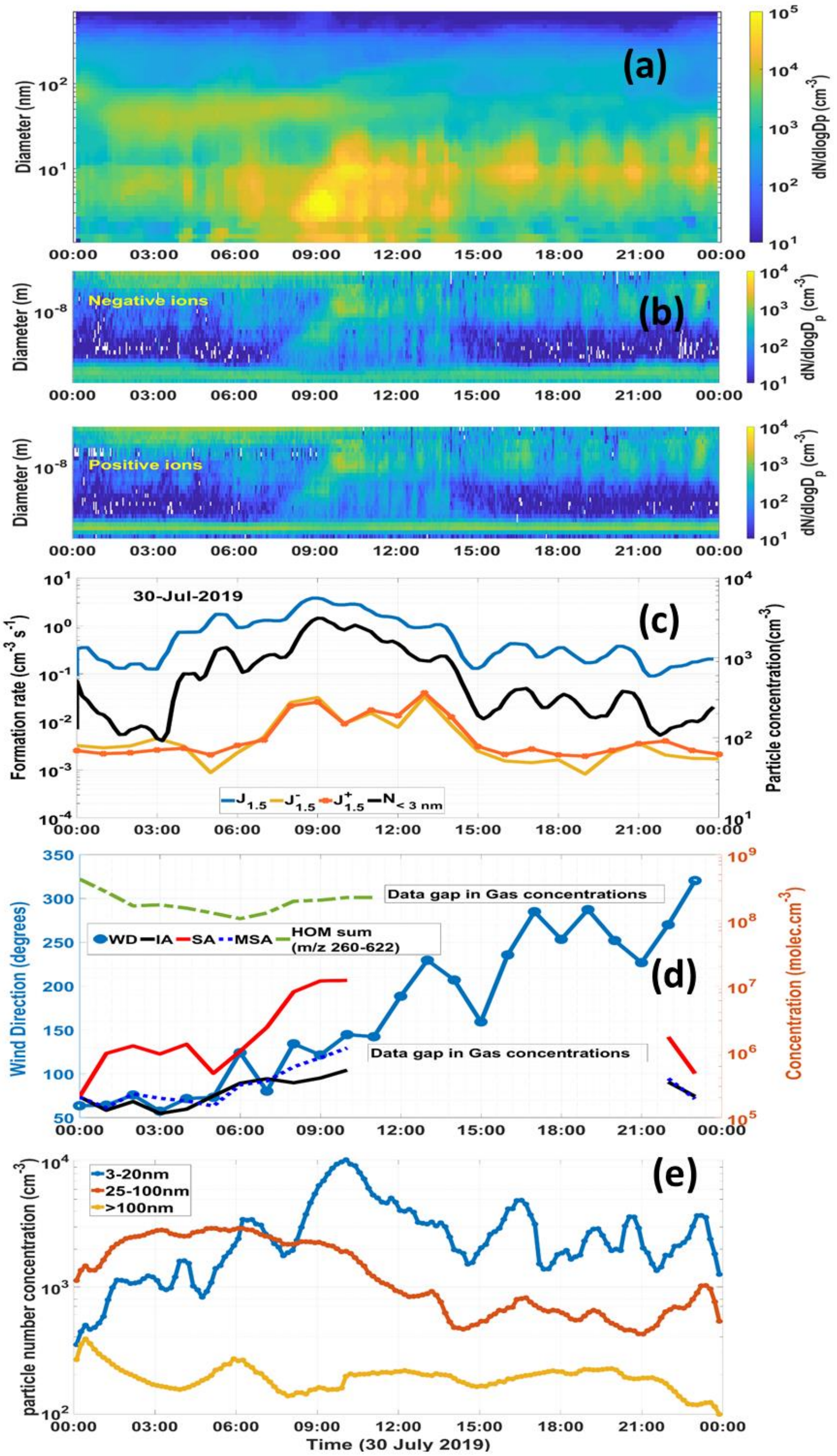

Figure S5: Local/regional Event, 30 July 2019. (a) Number size distribution of particles (data combined from PSM,NAIS and DMPS; size range: sub-3 nm–1000nm). (b) Charged particle number size distribution (negative: upper, positive: lower) obtained from the NAIS. (c) formation rates ($J_{1.5}$) of 1.5 nm particles and ions ($J^-_{1.5}$ and $J^+_{1.5}$) particle number concentrations (<3 nm). (d) Dirunal variation of HOMs, SA, IA and MSA with wind direction (WD). (e) The concentration of nucleation (3–10 nm) Aitken (10–100 nm) and accumulation mode (>100nm) particles during the event.

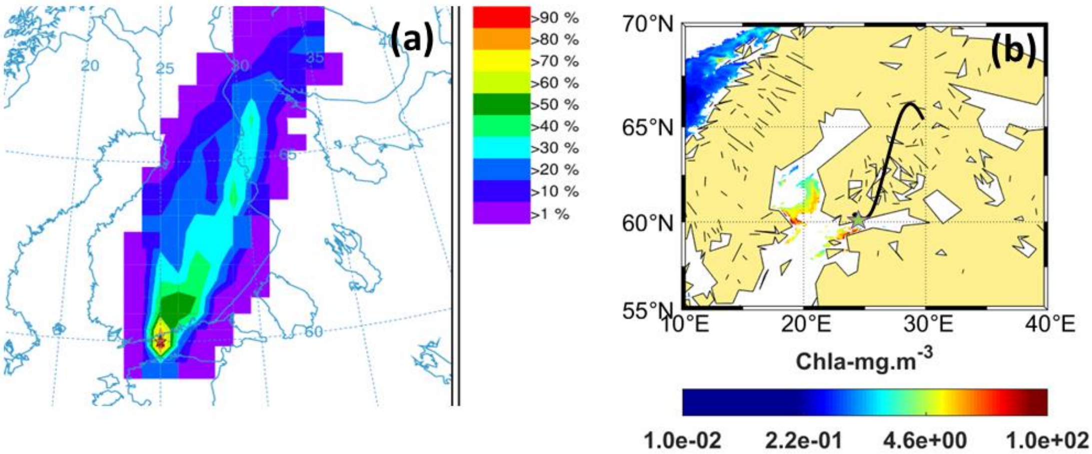

Figure S6: (a) Trajectory frequency plot (100 a.g.l, arrival time of trajectory at the measurement site: 22:00 h) for 24 h back trajectory using GDAS meterological input data (frequency grid resolution: $1.0^{\circ} \times 1.0^{\circ}$) (b) Chl-*a* concentrations (GlobColour level-3); Black line shows the trajectory direction and the star point denotes the measurement site.

Even in lakes the abundance of cynobacteria was sparse. Only cynobacterial bloom was found in Southern edge of Gulf of Bothania and northern most part of the Baltic sea. The trajectory frequency plots showed that most of the trajectories were from the northern land areas (including urban cities and boreal forests) of Finland (Fig. S5f) with highest residence times over these land regions. Therefore, the precursor gases from the biogenic origin, IA and MSA do not show a significant concentration increase as compared to SA, during this event and hence their contribution towards the initation of the NPF event may not be as significant as SA. The greater residence times over the land areas clearly support SA-driven NPF with possible contribution of organics.

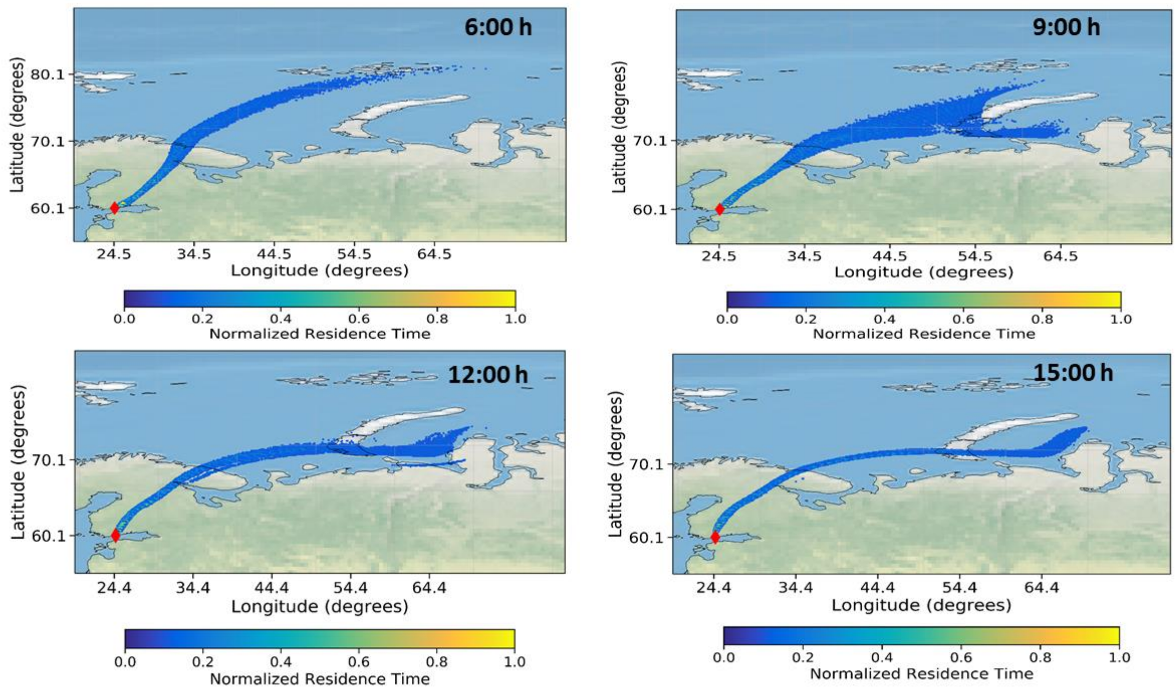

Figure S7: Normalized residence times of air masses (3-days backwards) arriving at the experimental site on 30 July 2019. The color bar indicates the normalized residence times for each subplot. The residence time of particles originating 3 days before reaching SMEAR III is shown for 6:00 h, 9:00 h, 12:00 h and 15:00 h. The red shaded areas indicate the latitude/longitude pairs having the maximum residence time. Note the highest residence times over the land areas.

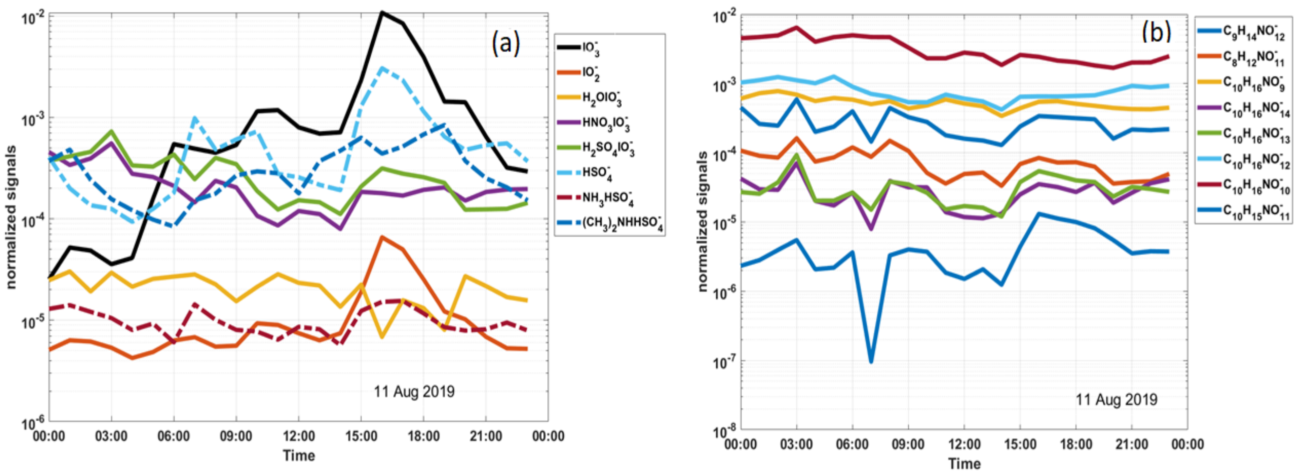

Figure S8: Diurnal variation of the inorganic (a) and organic clusters (b) observed during the NPF event on 11 August 2019.

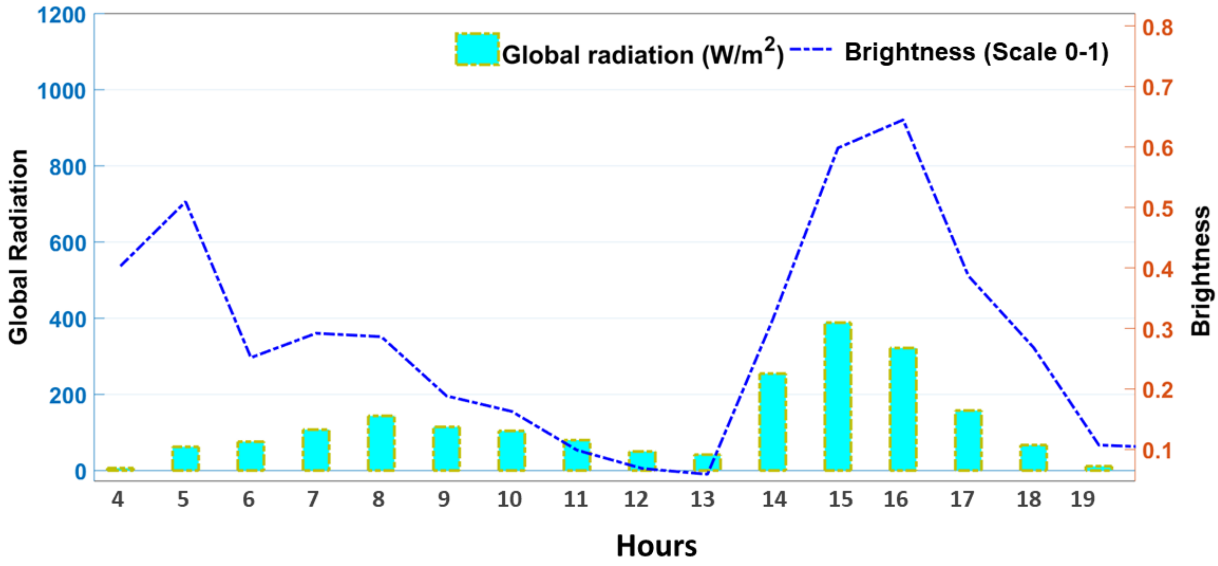

Figure S9: Diurnal variability of global radiation and estimated cloudiness on 11 August 2019. Note the increased radiation and brightness from 14–16 h (time when NPF starts).

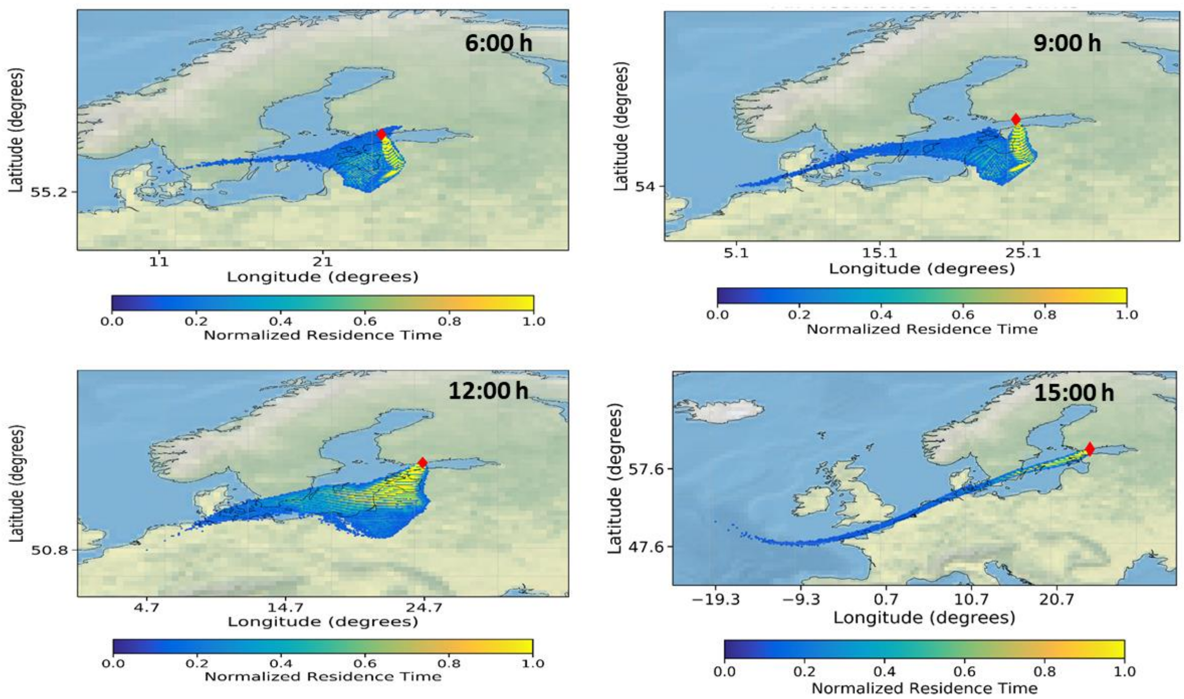

Figure S10: Normalized residence times of air masses (3-day backwards) arriving at the experimental site on 11 August 2019. The color bar indicates the normalized residence times for each subplot. The residence time of particles originating 3 days before reaching SMEAR III is shown for 6:00 h, 9:00 h, 12:00 h and 15:00 h. The red shaded areas indicate the latitude/longitude pairs having the maximum residence time. Note the highest residence times over Baltic Sea region at 15:00 h (highest IA concentration was observed).

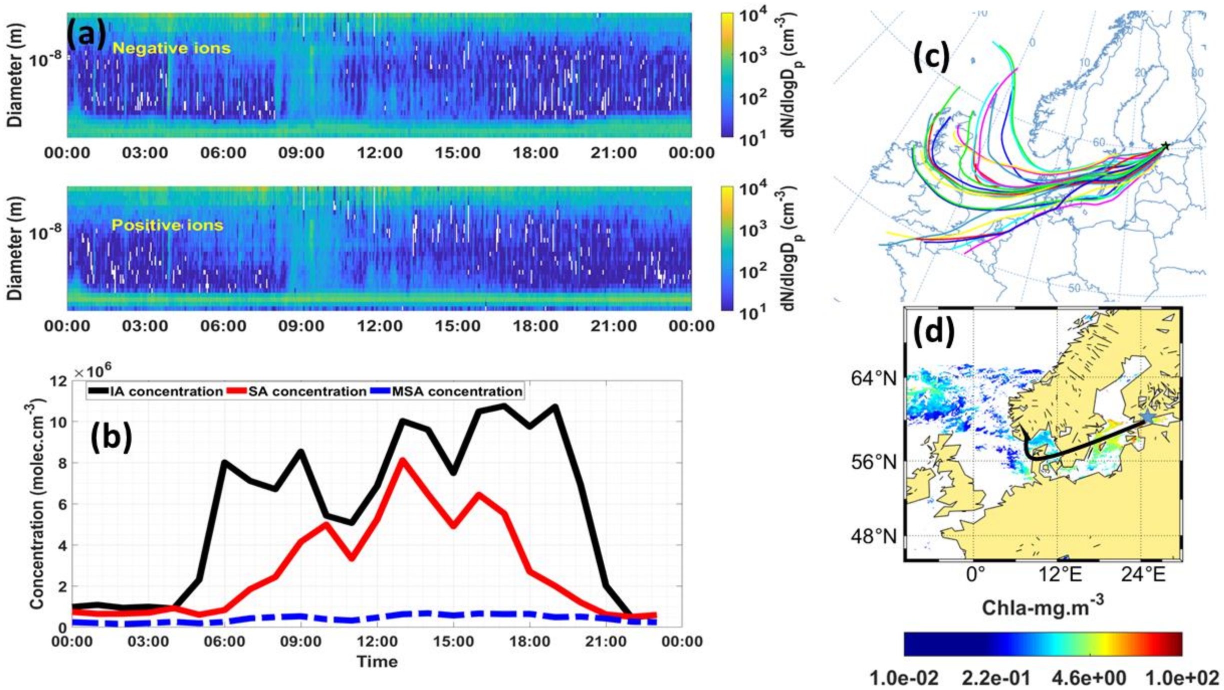

Figure S11: (a) Charged particle number size distribution (negative: upper, positive: lower) obtained from the NAIS. (b) concentration of SA, IA and MSA. (c) Trajectory analyis plot (100 a.g.l) for 24 h back trajectory using GDAS meterological input data (frequency grid resolution: 1.0° × 1.0°) (d) Chl-*a* concentrations (GlobColour level-3) for 14 August 2019. Black line shows the trajectory direction and the star point denotes the measurement site.

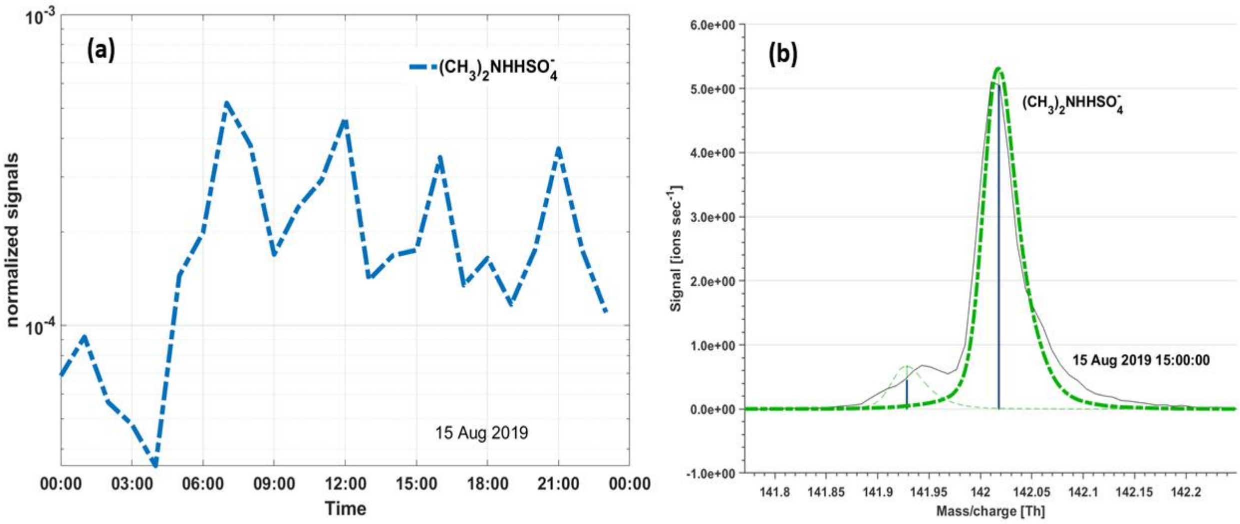

Figure S12: (a) Diurnal variation of the DMA-SA cluster (CI-ApiToF) observed during the NPF event on 15 August 2019. (b) The prominent peak of DMA-SA cluster seen at the peaktime of NPF at 15:00 h.

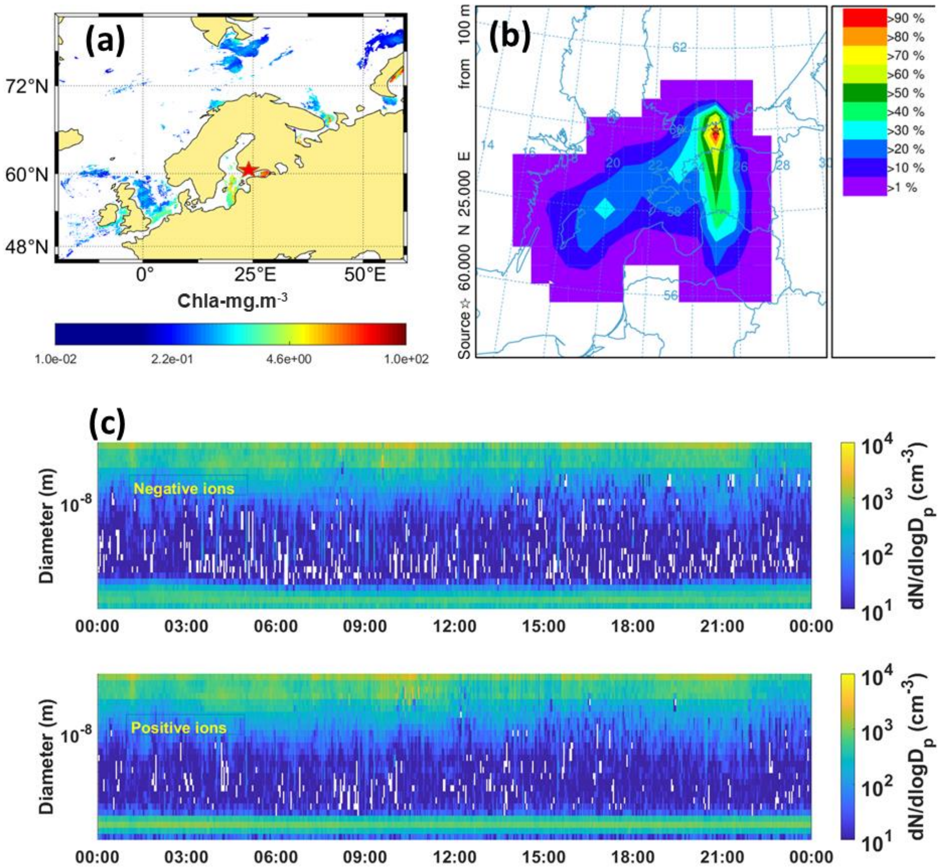

Figure S13: No event day, 17 August 2019 (a): Satellite map showing Chl*a* concentrations (GlobColour level-3) (b) Trajectory analyis plot (100 a.g.l) for 24 h back trajectory using GDAS meterological input data (frequency grid resolution: 1.0°×1.0°). (c) Charged particle number size distribution (negative: upper, positive: lower) obtained from the NAIS.

References:

Beck, L. J., Sarnela, N., Junninen, H., Hoppe, C. J. M., Garmash, O., Bianchi, F., Riva, M., Rose, C., Peräkylä, O., Wimmer, D., Kausiala, O., Jokinen, T., Ahonen, L., Mikkilä, J., Hakala, J., He, X. C., Kontkanen, J., Wolf, K. K. E., Cappelletti, D., Mazzola, M., Traversi, R., Petroselli, C., Viola, A. P., Vitale, V., Lange, R., Massling, A., Nøjgaard, J. K., Krejci, R., Karlsson, L., Zieger, P., Jang, S., Lee, K., Vakkari, V., Lampilahti, J., Thakur, R. C., Leino, K., Kangasluoma, J., Duplissy, E. M., Siivola, E., Marbouti, M., Tham, Y. J., Saiz-Lopez, A., Petäjä, T., Ehn, M., Worsnop, D. R., Skov, H., Kulmala, M., Kerminen,

V. M. and Sipilä, M.: Differing Mechanisms of New Particle Formation at Two Arctic Sites, Geophys. Res. Lett., doi:10.1029/2020GL091334, 2021.

Dada, L., Lehtipalo, K., Kontkanen, J., Nieminen, T., Baalbaki, R., Ahonen, L., Duplissy, J., Yan, C., Chu, B., Petäjä, T., Lehtinen, K., Kerminen, V. M., Kulmala, M. and Kangasluoma, J.: Formation and growth of sub-3-nm aerosol particles in experimental chambers, Nat. Protoc., 15(3), 1013–1040, doi:10.1038/s41596-019-0274-z, 2020.

Dal Maso, M., Liao, L., Wildt, J., Kiendler-Scharr, A., Kleist, E., Tillmann, R., Sipilä, M., Hakala, J., Lehtipalo, K., Ehn, M., Kerminen, V. M., Kulmala, M., Worsnop, D. and Mentel, T.: A chamber study of the influence of boreal BVOC emissions and sulfuric acid on nanoparticle formation rates at ambient concentrations, Atmos. Chem. Phys., 16(4), 1955–1970, doi:10.5194/acp-16-1955-2016, 2016.

Järvi, L., Hannuniemi, H., Hussein, T., Junninen, H., Aalto, P. P., Hillamo, R., Mäkelä, T., Keronen, P., Siivola, E., Vesala, T. and Kulmala, M.: The urban measurement station SMEAR III: continuous monitoring of air pollution and surface–atmosphere interactions in Helsinki, Finland. Boreal Environ. Res., 14 (suppl. A), 86–109, 2009.Kulmala, M., Petäjä, T., Nieminen, T., Sipilä, M., Manninen, H. E., Lehtipalo, K., Dal Maso, M., Aalto, P. P., Junninen, H., Paasonen, P., Riipinen, I., Lehtinen, K. E. J., Laaksonen, A. and Kerminen, V. M.: Measurement of the nucleation of atmospheric aerosol particles, Nat. Protoc., 7(9), 1651–1667, doi:10.1038/nprot.2012.091, 2012.

Lehtipalo, K., Kontkanen, J., Kangasluoma, J., Franchin, A., Wimmer, D., Schobesberger, S., Junninen, H., Petäjä, T., Sipilä, M., Worsnop, D. R., Kulmala, M., Lehtipalo, K., Mikkilä, J., Vanhanen, J., Leppä, J. and Worsnop, D. R.: Methods for determining particle size distribution and growth rates between 1 and 3 nm using the Particle Size Magnifier, Boreal Environ. Res., 19(September), 215–236, 2014.

Mangin., A. and d'Andon., O.F.: GlobColour Product User Guide, GC-UM-ACR-PUG-01, Version 4.1, 2017.

Nieminen, T., Lehtinen, K. E. J. and Kulmala, M.: Sub-10 nm particle growth by vapor condensation-effects of vapor molecule size and particle thermal speed, Atmos. Chem. Phys., doi:10.5194/acp-10-9773-2010, 2010.

Perez, R., Ineichen, P., Seals, R. and Zelenka, A.: Making full use of the clearness index for parameterizing hourly insolation conditions, Solar Energ., 45, 111–114, doi:10.1016/0038- 092X(90)90036-C, 1990.

Pisso, I., Sollum, E., Grythe, H., Kristiansen, N. I., Cassiani, M., Eckhardt, S., Arnold, D., Morton, D., Thompson, R. L., Groot Zwaaftink, C. D., Evangeliou, N., Sodemann, H., Haimberger, L., Henne, S., Brunner, D., Burkhart, J. F., Fouilloux, A., Brioude, J., Philipp, A., Seibert, P. and Stohl, A.: The Lagrangian particle dispersion model FLEXPART version 10.4, Geosci. Model Dev., doi:10.5194/gmd-12-4955-2019, 2019.

Rolph, G., Stein, A. and Stunder, B.: Real-time Environmental Applications and Display sYstem: READY, Environ. Model. Softw., 95, 210–228, doi:10.1016/j.envsoft.2017.06.025, 2017.

Sánchez, G., Serrano, A., and Cancillo, M.: Effect of cloudiness on solar global, solar diffuse and terrestrial downward radiation at Badajoz (Southwestern Spain), Optica pura y aplicada, 45, 33– 38, 2012.

Sogacheva, L., Saukkonen, L., Nilsson, E., Dal Maso, M., Schultz, D. M., De Leeuw, G., and Kulmala, M.: New aerosol particle formation in different synoptic situations at Hyytiälä, southern Finland, Tellus B, 60, 485–494, doi:10.1111/j.1600- 0889.2008.00364.x, 2008.

Stein, A. F., Draxler, R. R., Rolph, G. D., Stunder, B. J. B., Cohen, M. D. and Ngan, F.: Noaa's hysplit atmospheric transport and dispersion modeling system, Bull. Am. Meteorol. Soc., 96(12), 2059–2077, doi:10.1175/BAMS-D-14-00110.1, 2015.

Stohl, A., Forster, C., Frank, A., Seibert, P. and Wotawa, G.: Technical note: The Lagrangian particle dispersion model FLEXPART version 6.2, Atmos. Chem. Phys., doi:10.5194/acp-5-2461-2005, 2005.

Stolzenburg, D., Stolzenburg, D., Simon, M., Ranjithkumar, A., Kürten, A., Lehtipalo, K., Lehtipalo, K., Gordon, H., Ehrhart, S., Finkenzeller, H., Pichelstorfer, L., Nieminen, T., He, X. C., Brilke, S., Xiao, M., Amorim, A., Baalbaki, R., Baccarini, A., Beck, L., Bräkling, S., Murillo, L. C., Chen, D., Chu, B., Dada, L., Dias, A., Dommen, J., Duplissy, J., El Haddad, I., Fischer, L., Carracedo, L. G., Heinritzi, M., Kim, C., Kim, C., Koenig, T. K., Kong, W., Lamkaddam, H., Lee, C. P., Leiminger, M., Leiminger, M., Li, Z., Makhmutov, V., Manninen, H. E., Marie, G., Marten, R., Müller, T., Nie, W., Partoll, E., Petäjä, T., Pfeifer, J., Philippov, M., Rissanen, M. P., Rissanen, M. P., Rörup, B., Schobesberger, S., Schuchmann, S., Shen, J., Sipilä, M., Steiner, G., Stozhkov, Y., Tauber, C., Tham, Y. J., Tomé, A., Vazquez-Pufleau, M., Wagner, A. C., Wagner, A. C., Wang, M., Wang, Y., Weber, S. K., Wimmer, D., Wimmer, D., Wlasits, P. J., Wu, Y., Ye, Q., Zauner-Wieczorek, M., Baltensperger, U., Carslaw, K. S., Curtius, J., Donahue, N. M., Flagan, R. C., Hansel, A., Hansel, A., Kulmala, M., Lelieveld, J., Volkamer, R., Kirkby, J., Kirkby, J. and Winkler, P. M.: Enhanced growth rate of atmospheric particles from sulfuric acid, Atmos. Chem. Phys., doi:10.5194/acp-20-7359-2020, 2020.